Flow Analysis of Hammerhead Launcher Geometries in the Transonic Regime

D'aguanno, Alessandro; Romero, Andrea González; Schrijer, Ferry; van Oudheusden, Bas

Important note
To cite this publication, please use the final published version (if applicable).
Please check the document version above.

Flow Analysis of Hammerhead Launcher Geometries in the Transonic Regime

Alessandro D'Aguanno,* Andrea González Romero,† Ferry Schrijer,‡ and Bas van Oudheusden§
Delft University of Technology, 2629 HS Delft, The Netherlands

Hammerhead launcher configurations, characterized by a larger diameter in the payload fairing than the rest of the launch vehicle, face substantial challenges during transonic operations due to their susceptibility to flow separation. This experimental study investigates the influence of the nose and boat tail geometry on the flow around hammerhead configurations in the transonic regime ($Ma = 0.7–0.8$) and for various angles of attack ($\alpha = 0–4°$). To gain a general understanding of the shockwave structures, flow separation and reattachment, oil flow and schlieren visualizations were employed. Schlieren visualizations were also utilized to characterize the level of unsteadiness in these regions. Additionally, particle image velocimetry was employed to quantify variations in the velocity field. The study's findings reveal an optimization of flow performance in the presence of a bi-conic nose, attributed to the creation of two-shockwave structures with relatively low intensity. This is in contrast to the ogive and conic noses, which exhibit a single, more detrimental shockwave structure. The investigation into different boat tail angles indicates that adopting low-angle boat tails (5° and 15° compared to 34°) leads to a noticeable reduction in the separated area, albeit associated with an increase in the range of oscillation of the shockwave structures.

I. Introduction

AS THE demand for reusable launch vehicles increases, a renewed interest in hammerhead or payload fairing (PLF) configurations has emerged. Hammerhead configurations consist of a nose cone, a payload compartment, and a boat tail (BT) region, as illustrated in Fig. 1 and are characterized by a larger diameter in the payload area than in the rest of the launch vehicle (LV), enabling the reuse of the same LV for a range of payload sizes. Industry leaders such as the European Space Agency's Vega-C launcher as well as the SpaceX's Falcon launchers have adopted these designs, demonstrating their relevance and effectiveness.

Among the different regimes that payload fairings face during flight, the transonic is relevant as flow separation may be induced by geometries as the hammerhead, exposing the vehicle to intense pressure fluctuations and to the external intense acoustic pressure field [1] characteristic of this flight phase. The unsteady loads exhibit pressure fluctuations with different frequency contents, ranging from low to extremely high frequencies. As a result, documenting and understanding the complex flow phenomena around hammerhead PLFs is essential for developing more efficient and reliable launch vehicles [1,2].

The boat tail region, which connects the cylindrical portion of the fairing to the rest of the launcher (see Fig. 1), is particularly prone to inducing flow separation, resulting in a reverse flow region. The flow in the boat tail region exhibits characteristic features of a backward-facing step geometry: shear layer separation, a recirculation region, and a reattachment location. The flow separation induced by the boat tail region leads to prominent levels of low-frequency wall pressure fluctuations (buffet) and may also induce shock wave-boundary layer interaction [3–5]. For launchers in the transonic regime, the typical Strouhal numbers (based on the model diameter) for the pressure fluctuation in the boat tail area are in the order of 0.1 to 0.3 [6].

The separated boat tail flow can reattach downstream of the boat tail due to the long, relatively uniform cylindrical region that follows the hammerhead shape. This phenomenon is significant and must be considered during the design of hammerhead payload geometries, as it can impact both the vehicle's aerodynamic performance and its structural integrity. The importance of studying hammerhead wake reattachment has been emphasized by Ericsson [7], suggesting that this phenomenon may cause aeroelastic instability for the lowest bending modes of the structure.

Therefore, it is evident that the forebody configuration of a launch vehicle plays a critical role during the ascent phase, significantly influencing the aerodynamic flow behavior throughout atmospheric flight and contributing heavily to buffet effects. To mitigate these challenges, NASA compiled findings from various experimental investigations into a comprehensive handbook [8], which outlines general design guidelines for achieving a buffet-free configuration.

Several numerical studies are also accessible on this topic, including those by Camussi et al. [9], Imperatore et al. [10], Kim et al. [11], Panda [12], and Troclet and Depuydt [13]. These studies often rely on Reynolds-Averaged Navier-Stokes (RANS) turbulence models (due to computational limitations), despite their limited ability to capture the unsteadiness characteristic of such flows. However, several studies employing hybrid RANS/Large Eddy Simulations (LES) techniques, which model parts of the flow field (e.g., the separated regions) using LES, are also available, such as those by Liu et al. [14], Murman and Diosady [15] and Lecler et al. [16]. More recently, a transonic hammerhead configuration has been investigated using a wall-modeled LES approach, as shown by Kenway et al. [17]. This study demonstrated good agreement with experimental data (Schuster et al. [18]) regarding pressure fluctuations in the payload fairing but exhibited larger discrepancies in quieter regions, such as the nose area of the fairing. Given the limitations of numerical approaches and the need for further validation and insights into this flow configuration, experimental investigations remain of great interest and are the focus of this study.

In terms of design, there are various nose shapes for payload fairings, with the conic and ogive shapes being the most frequently used [19]. The bi-conic nose results in an improved aerodynamic performance compared to the conic nose, since it prevents a sudden change of flow separation topology (which also results in a smoother

*Guest Researcher, Aerodynamics Section, Department of Flow Physics and Technology; also Research Engineer in Experimental Aerodynamics, Turbomachinery and Propulsion Department, von Karman Institute for Fluid Dynamics, 1640 Sint-Genesius-Rode, Belgium; A.Daguanno@tudelft.nl (Corresponding Author).

†Former Graduate MSc Student, Aerodynamics Section, Department of Flow Physics and Technology.

‡Assistant Professor and Scientific Director of the FPT Lab, Aerodynamics Section, Department of Flow Physics and Technology.

§Associate Professor, Aerodynamics Section, Department of Flow Physics and Technology.
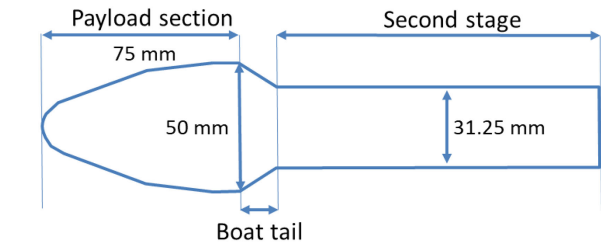
Fig. 1 Geometry of a hammerhead launcher (bi-conic nose and 34° boat tail).

hammerhead wake reattachment) [7]. Other possible shapes are elliptical, parabolic, and Sears-Haack (SH) ogive shapes (see Fig. 2 for possible nose geometries). The Sears-Haack shapes are particularly interesting as they are mathematically derived to minimize drag. In fact, the SH nose also has the advantage of gradually expanding the flow, resulting in a weaker terminal shockwave (SW) on the fairing.

Similarly, also the boat tail shape is a very relevant aspect of the launcher forebody geometry, in view of its influence on the separated area extent and the reattachment location. Numerous studies have been conducted to analyze and characterize the flow around boat tails, mostly focusing on conventional conical boat tail configurations. For instance, Medeiros et al. [1] and Kumar et al. [20] conducted experimental investigations in the transonic regime to assess the impact of several boat tail angles (8°, 16°, and 90° in [1] and 15°, 31.5° and 90° in [20]) on hammerhead PLFs with a generic ogive shape nose or the VLS-1 shape, respectively. For the range of Mach numbers and model configurations studied by Kumar et al. [20], two types of boat tail flows were observed: one where the boundary layer separation occurred at the boat tail corner with shear layer reattachment downstream on the cylinder surface (Type I) and another where the shock-induced boundary layer separation occurred along the boat tail with subsequent reattachment on the cylinder surface (Type II) for very few cases.

Although in more recent years many studies are considering the impact of the boat tail geometry on the launcher performance [21,22], none of these studies has considered the specific impact of the nose geometry and instead use a generic design. For example, several papers in the literature have used the so-called Model 11 hammerhead configuration, such as in the studies of Coe and Nute [3], Kim et al. [11], Liu et al. [14], Panda et al. [23], and Murman and Diosady [15]. For this reason, this configuration (consisting of a bi-conic nose and a boat tail of 34°) has become a benchmark for launcher aerodynamics studies.

Notwithstanding the wide consensus for this configuration, the nose section's design significantly impacts the PLF's aerodynamic performance, and although many studies have considered this effect, a research gap is identified, as prior studies have not compared nose shapes under the same geometrical and flow conditions. For instance, Coe's [19] and Ericsson and French's [24] studies are not directly comparable. This limitation hinders the ability to draw reliable conclusions about the effect of nose shape on aerodynamic performance. Furthermore, most existing studies focus on either nose or boat tail geometry in isolation.

Therefore, the goal of this study is to compare different launcher geometry configurations and to investigate the effect of the nose shape and the boat tail shape for different flow conditions (Mach number and angle of attack). By means of this analysis, the interaction of the specific nose and boat tail configuration on the separated area and the relative reattachment in the boat tail region are explored. This study also aims to investigate whether the choice of a specific payload fairing influences the boat tail flow field and vice versa. Additionally, high-fidelity flow-field data collected using particle image velocimetry (PIV), a technique rarely employed in hammerhead studies, will provide further insights into the flow physics of this phenomenon. These data will also enable more direct and meaningful comparisons with numerical studies.

II. Experimental Investigation

A. Facility

The current experimental study was carried out in the transonic-supersonic wind tunnel (TST 27) at TU Delft. The wind tunnel is a blow-down type with a test section measuring 25.5 cm in height and 28 cm in width.

Experiments were conducted with a total pressure (p_0) of 2 bars, a total temperature (T_0) of 293 K, and a Mach number range (Ma) of [0.7–0.8]. The flow conditions are also summarized in Table 1.

To enhance the quality of schlieren and PIV images, solid walls were employed in the wind tunnel test section. This choice introduces a non-negligible blockage effect compared to slotted walls, leading to an expected increase in the actual freestream Mach number beyond the set value.

B. Launcher Models

The wind tunnel models used in this study are based on the Model 11 of Coe and Nute [3], which is commonly employed as a reference for validating results related to hammerhead PLF aerodynamics in the transonic regime (as seen in Panda et al. [23]). This model features a spherically blunted bi-conic nose and a conical boat tail of 34°, and a sketch of the model is depicted in Fig. 1, along with some characteristic dimensions.

Different launcher models have been produced and investigated by varying two geometrical parameters:
1) Nose shape geometry;
2) Boat tail angle.

Regarding the nose shape geometry, three configurations are considered: a Sears-Haack (SH) nose cone optimized for drag minimization, and conic (C) and bi-conic (BC) nose shapes (see Fig. 2).

Table 1   Flow conditions

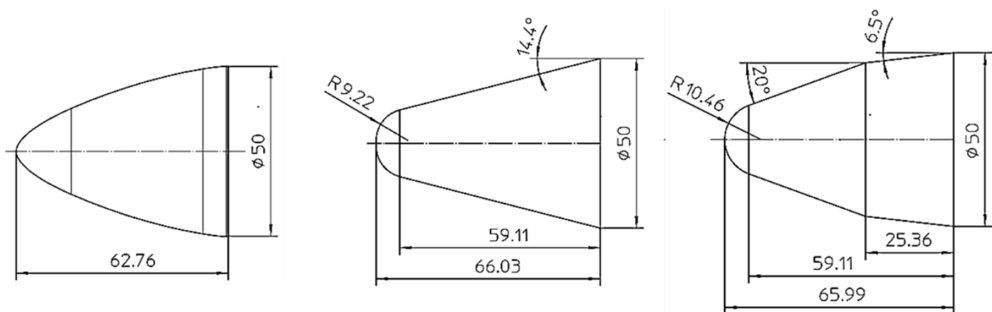| Parameter	Symbol	Value
Free stream Mach number	Ma_∞	0.7; 0.8
Angle of attack	α	0°; 4°
Total temperature	T_0	293 K
Total pressure	p_0	2 bar
Reynolds number based on model diameter	Re_D	$1.37 \cdot 10^6$

Fig. 2   CAD drawings of the different nose geometries: Sears-Haack (left), conic (center), and bi-conic (right) noses.

Table 2 Geometrical properties of launcher models

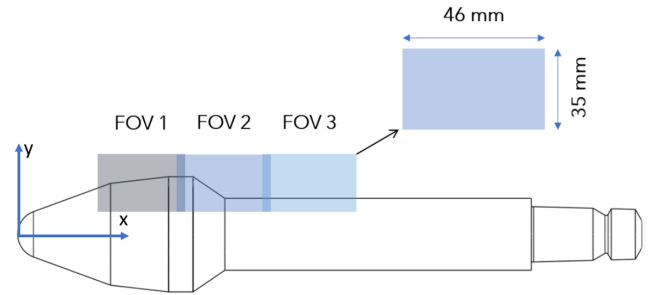| Parameter	Symbol	Value
Payload section diameter	D	50 mm
Second stage diameter	d	31.25 mm
Noses configurations	——	Bi-conic, Conic, Sears Haack
Boat tail configurations	BT	5°; 15°; 34°
Payload/nose section length	l_{PL}	77 mm
Second stage length (with BT)	$l_{2°S}$	148 mm

All nose shapes share equal length (77 mm) and maximum diameter D (50 mm) and are connected to the cylindrical (and boat tail) section, serving as the main element of the model, with a diameter $d = 31.25$ mm (resulting in a step height $h = 0.1875D = 9.375$ mm). The various geometrical properties of the launcher models are also summarized in Table 2. Between the SH shape and the conic nose [2], the former offers advantages such as greater internal volume for accommodating payload, reduced drag, and minimized unsteady aerodynamic loads. However, the conic nose is simpler to manufacture and less prone to manufacturing defects. To mitigate the drawbacks of the conic nose while maintaining manufacturing simplicity, the bi-conic nose is often preferred. The bi-conic configuration offers an advantage over the conic nose by preventing flow separation at the cone-cylinder junction due to its gentler angle transition. Thus, in addition to representing common payload fairing shapes, these three nose configurations were selected to highlight variations in the key statistics associated with shockwave structures and the separated flow region over the boat tail.

For the boat tail area, the ratio $D/d = 1.6$ is kept constant, and three linear boat tails were manufactured (see Fig. 3) with angles of 5°, 15°, and 34° (the latter corresponding to the angle of the Coe and Nute model). These angles were chosen considering observed phenomena for different boat tail angle ranges: below 5°, a weak shockwave (SW) appears along the boat tail; between 5° and 30°, a shock-induced separated flow is present on the boat tail, leading to high loads [2]; beyond 30°, a no-shockwave separated flow exists over a long zone (similarly to a background facing step case).

Finally, an investigation of the Mach number and angle of attack effects is conducted to isolate the conditions for higher unsteadiness. Test conditions include two angles of attack $\alpha = [0°; 4°]$ and two Mach numbers $Ma = [0.7; 0.8]$. The choice of these parameters is based on other studies, such as in Panda et al. [23] and Garbeff et al. [25]. Furthermore, the presence of an angle of attack is often studied since, in ascent conditions, a launcher normally experiences angles of attack in the range $\pm 6°$ [2].

The models are attached to a cylindrical sting (see Fig 4) connected to a model support, which is clamped to the bottom wall of the wind tunnel (downstream of the test section) and allows for the variation of the angle of attack.

The tests ($Ma = 0.8$ and $D = 50$ mm) have been carried out with $Re_D = 1.37 \cdot 10^6$, which is significantly lower than the Reynolds number reported under flight conditions for a launcher during the initial high transonic flight phase, where values of approximately 35×10^6 [26] are observed. However, it is important to note that, in this specific study, a transition trip was implemented at 20% of the nose length to ensure that turbulent boundary layer transition

Fig. 4 Sketch of experimental model (Coe and Nute configuration) and relative PIV FOVs.

occurs at approximately the same location as in-flight conditions. This position corresponds to approximately 5% of the entire model length, as suggested by Pope and Goin [27]. In this study, the transition trip consists of a strip of 1.5 mm width with carborundum particles (particle size of 0.014 mm). These particles have been previously demonstrated to be effective in ensuring a turbulent boundary layer in other transonic applications [28]. In the study by Nicolì et al. [26], the effect of Reynolds number was examined in detail, addressing the extrapolation of aerodynamic coefficients from ground-based experiments to flight conditions. The results indicate that in the transonic regime (excluding $0.95 < Ma < 1.1$), the flow topology appears to be largely independent of Reynolds number with a variation of approximately 0.01 in the normal aerodynamic coefficient across a Reynolds number range of $1 \times 10^6 < Re < 50 \times 10^6$. Thus, Reynolds number effects are not expected to influence the results of this study.
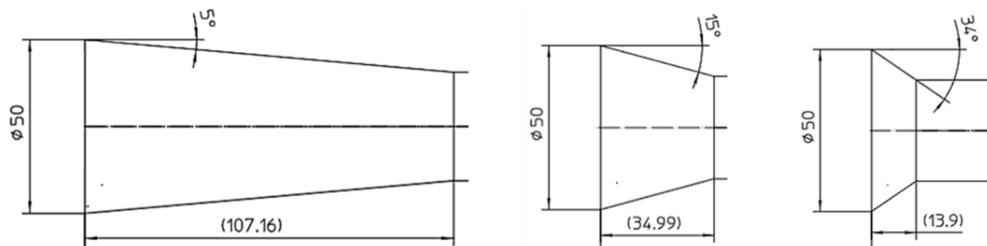
C. Experimental Setup

The experiments employed three optical techniques: oil flow visualization, schlieren, and particle image velocimetry (PIV).

Oil flow visualizations provided a qualitative insight into the flow field with main focus on observing flow transition, shockwave location, the extent of the separated area, and reattachment location. In this study, the oil was produced using Shell oil Tellus 29 mixed with TiO_2 particles and oleic acid.

To capture the unsteady nature of the flow field, the schlieren technique was utilized with a z-configuration [29]. The schlieren setup included an LED lamp and a high-speed recording camera. A Photron Fastcam SA1.1 camera with a 5 kHz acquisition frequency was used, providing sufficient time resolution for capturing the flow unsteadiness. An exposure time of 49 μs was selected to freeze the flow structures adequately, while the camera's 8 GB memory allowed for a total acquisition time of 1.09 seconds (5457 images). The horizontal orientation of the knife edge (50% obstruction) was chosen to resolve density gradients associated with both the separated area and the shockwave structures. The field of view (FOV) of the schlieren image extends from well upstream of the model to the entire model length, including reattachment location. Furthermore, the FOV covered both the top and bottom sides of the model to highlight potential flow asymmetries in the presence of angle of attack.

After identifying the most relevant flow conditions from the schlieren measurements, planar-PIV tests were conducted using the setup depicted in Fig. 5 (left).

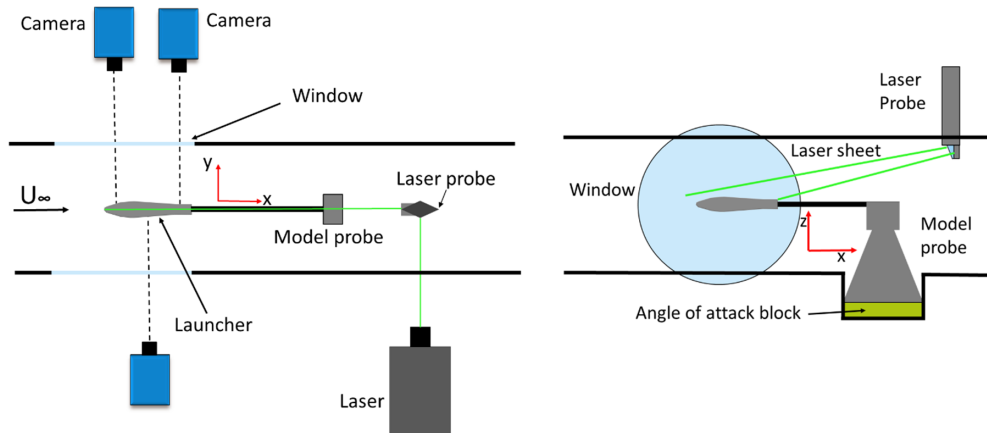**Fig. 3 CAD drawings of the different boat tail geometries: 5° (left), 15° (center), and 34° (right) boat tails.**

Fig. 5   Top (left) and side view (right) of PIV setup.

Three Bobcat Imperx IGV-B1610 cameras, each with a resolution of 1628×1236 pixels and a pixel size of 4.4 μm, were utilized. The cameras were fitted with 75 mm lenses featuring an f-stop of 3.9. The cameras acquired 250 images for each run (two runs were performed for each test case to achieve satisfactory statistics). Operating in double pulse mode with a pulse separation of $dt = 1.5$ μs, the cameras were arranged in a planar configuration to enhance spatial resolution. This arrangement resulted in a field of view of 46 mm in length and of 35 mm in height in the chordwise-vertical plane for each camera (see Fig. 4). As illustrated in Fig. 4, one camera was centered in the nose area, while the other two were positioned at the boat tail region to visualize both the separated area and the reattachment location. This configuration extended the FOV from $x/D = 50\%$ to $x/D = 300\%$, with the origin of the coordinate systems (for both the streamwise (x) and vertical axis (y)) located at the leading edge of the launchers' nose for all the configurations, with and without angle of attack, as shown in Fig. 4.

DEHS (Di-Ethyl-Hexyl-Sebacat) droplets served as seeding particles, possessing a relaxation time of 2 μs. The particles were illuminated in a 1.5 mm thick light sheet generated by a dual-cavity laser (Nd:YAG Spectra Physics Quanta Ray PIV-400). The laser operated at a repetition frequency of 5 Hz, a power of 400 mJ per pulse, a pulse duration of 6ns, and a wavelength of 532 nm. The laser beam was introduced into the wind tunnel test section using a laser probe, accessed from the top wall of the wind tunnel (see Fig. 5, right). To ensure synchronization between cameras and the laser, a LaVision programmable time unit was used.

D.   Processing Procedures and Uncertainties

The PIV images were acquired and processed in Davis 8.4. To reduce laser reflections on the model, a time minimum subtraction was implemented. Following that, a cross-correlation procedure was applied using a multipass approach, starting with a window size of 128×128 pixels and subsequent steps using a circular window size of 48×48 pixels. A window overlap of 75% resulted in a final vector spacing of 0.34 mm (0.7% of D). The universal outlier detection method [30] with a threshold value of 2 was utilized to eliminate potential outliers. Further processing of PIV, oil flow, and schlieren data was conducted using MATLAB®.

It is important to acknowledge and quantify some of the measurement uncertainties that affect the results, which have been collected in Table 3. The cross-correlation procedure described has an uncertainty in the estimation of the velocity field, which, for planar PIV, is lower than 0.1 pixels. Considering the specific pulse separation and magnification factor [31], an error lower than 2 m/s is expected.

Additionally, the DEHS particles, due to their relaxation time (2 μs, see [32]), may not accurately follow flow streamlines in the presence of strong velocity gradients. In this study, this effect is only relevant in correspondence of the shockwave structures, where it

Table 3   Measurement techniques parameters and uncertainties

Parameter	schlieren	PIV
Camera	$1 \times$ Photron SA1.1	$3 \times$ Bobcat Imperx
Acquisition frequency	5000 Hz	5 Hz
Number of images per test case	5000	500
Combined resolution	1008×468 pix	4884×1236 pix
Exposure time/ pulse separation	49 μs / -	- / 1.5μs
Final window size	— —	48×48 pix
Window overlap	— —	75%
Pixel/vector spacing	0.23 mm	0.34 mm
Cross-correlation uncertainty	— —	<2 m/s
Particle slip uncertainty	— —	<50 m/s (in SW)
Line of sight uncertainty	<1.5 mm	— —

could introduce uncertainty as high as 50 m/s. However, this effect is negligible in the remaining FOV.

Regarding the schlieren images, the higher uncertainty is associated with the presence of three-dimensional effects, which get integrated along the line of sight. The resulting uncertainty can be estimated as half of the thickness of the projected shockwave, thus being lower than 1.5 mm.
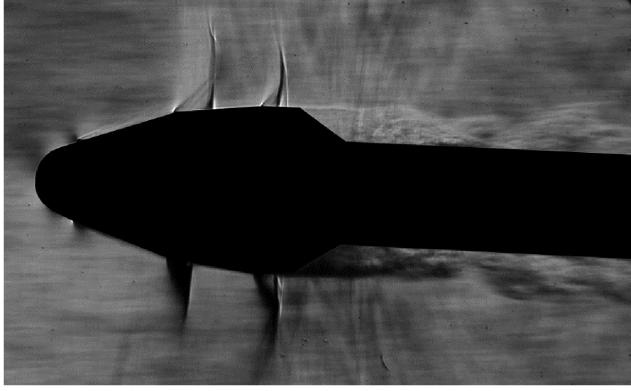
For a detailed explanation of the formulations related to the uncertainties mentioned, the reader is referred to the study by D'Aguanno et al. [33].

III.   Results

A.   Flow Field Characterization

Before delving into the detailed effects of geometry, the flow field around the Coe and Nute Model 11 geometry (bi-conic nose and boat tail of 34°) is first discussed in detail for an angle of attack of 4° and Mach number $Ma = 0.8$. The choice of this specific angle of attack is based on its significant attention in prior studies (refer to [3,17,18,23]). Similarly, the choice of $Ma = 0.8$ is justified by the studies of [23,34], who showed that the most critical flow condition occurs at this Mach number,while a further increase in Ma leads to a reduction in pressure fluctuations.

The primary flow features of the model investigated in this study are clearly observable through instantaneous schlieren and average PIV images (see Figs. 6 and 7). Two shockwaves are observed downstream of the two geometrical transitions present at the junction of the two conical sections and in the cone-cylinder junction. Expansion fans are present at these junctions, leading to the occurrence of supersonic areas, visible as oblique lines in the schlieren image and through a sharp increase in velocity in the PIV average flow field. The first shockwave is located at around $x/D = 92\%$ and the second just upstream of the boat tail region, at $x/D = 139\%$ (see also Table 4).

Fig. 6   Schlieren instantaneous image for $Ma = 0.8, \alpha = 4°$ on Coe and Nute configuration.

Table 4   Average location ($\overline{X_{SW}}$) of 1st and 2nd shockwave and relative ranges of oscillation (ΔX_{SW}).

Nose	BT, °	Ma	α, °	$\overline{X_{SW1}}/D$, %	$\overline{\Delta X_{SW1}}/D$, %	$\overline{X_{SW2}}/D$, %	$\overline{\Delta X_{SW2}}/D$, %
BC	5	0.7	0	81	6	— —	— —
BC	5	0.8	0	91	18	148	36
BC	15	0.7	0	81	6	128	4
BC	15	0.8	0	91	22	148	36
BC	34	0.7	0	83	8	132	6
BC	34	0.8	0	92	20	139	22
SH	5	0.7	0	124	8	— —	— —
SH	5	0.8	0	146	32	— —	— —
SH	34	0.7	0	122	6	— —	— —
SH	34	0.8	0	141	24	— —	— —
C	34	0.7	0	133	10	— —	— —
C	34	0.8	0	146	32	— —	— —
BC	5	0.7	4	85	8	131	2
BC	5	0.8	4	98	19	150	36
BC	15	0.7	4	85	6	133	2
BC	15	0.8	4	98	16	149	28
BC	34	0.7	4	85	8	132	4
BC	34	0.8	4	98	20	144	20
SH	34	0.7	4	122	6	— —	— —
SH	34	0.8	4	141	24	— —	— —
C	34	0.7	4	138	12	— —	— —
C	34	0.8	4	152	22	— —	— —

While some vortex dynamics are observable in the schlieren image in the boat tail area, quantitative information cannot be obtained because of the spanwise integration effect. However, the PIV average field clearly shows the presence of a separated area triggered at the boat tail top corner. The flow streamlines show the presence of a recirculation area downstream of the boat tail top corner, resulting in a positive vertical velocity along the boat tail oblique edge and a negative velocity further downstream.

Separated flow triggered at the boat tail top corner is also visible from the oil flow visualization in Fig. 8. The reattachment location is clearly visible and consistent along the entire circumferential direction of the model, with the curvature of the oil flow pattern induced by the presence of the angle of attack.

The location of the reattachment location (L) was obtained from both PIV (L_{PIV}) and the oil flow visualization (L_{OIL}), obtaining: $L_{PIV} = 86\%D$, while $L_{OIL} = 104\%D$ (see Table 5); therefore, the PIV value tends to underestimate the reattachment location when compared to the oil flow data. This discrepancy is primarily associated with the fact that PIV does not directly measure on the model's surface but rather at a certain distance from it due to laser reflections. However, it cannot be ruled out that the oil flow visualization may also perturb the separated area as observed by Nicolì et al. [26] by comparing schlieren and oil flow images.
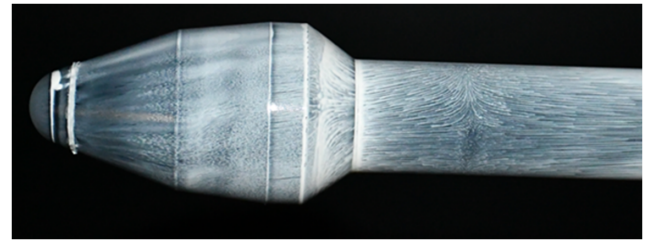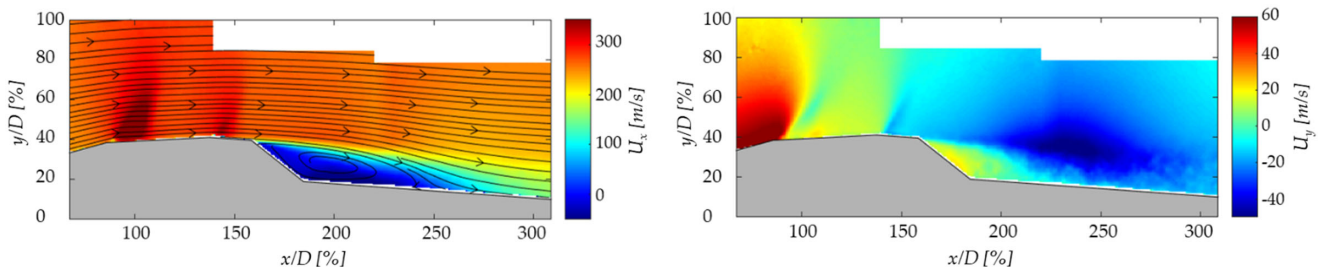
On the nose cone, further perturbations associated with the presence of a transition trip are observed, visible in both the oil flow visualization and schlieren image.

To quantify the unsteadiness in the flow field, the standard deviation (σ) of both the schlieren intensity count and the horizontal PIV velocity component is shown in Fig. 9. Velocity fluctuations in the first shockwave oscillation range are well aligned with the schlieren intensity counts counterpart. However, the second shockwave oscillation range appears reduced in the PIV image, potentially indicating 3D effects integrated along the line of sight, unique to schlieren images.

In addition to the velocity fluctuations in the shockwave oscillation ranges, Fig. 9 (right) also highlights fluctuations of velocity in the boat tail region and downstream of it, with the highest values in
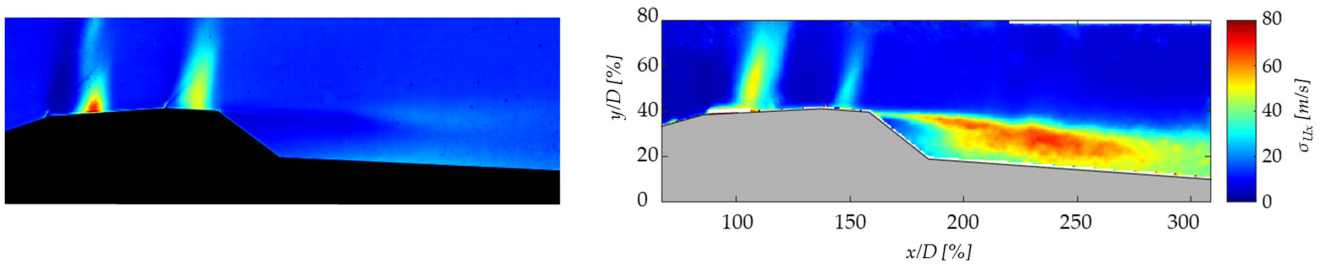

Fig. 8   Oil flow visualization for $Ma = 0.8, \alpha = 4°$ on Coe and Nute configuration.

Table 5   Reattachment location from oil flow and PIV measurements

Nose	BT, °	Ma	α, °	L_{OIL}/D	L_{PIV}/D
BC	34	0.7	0	0.94	0.79
BC	34	0.8	0	0.94	0.79
SH	34	0.8	0	0.92	— —
C	34	0.8	0	1.32	— —
BC	34	0.7	4	0.90	— —
BC	34	0.8	4	1.04	0.86
BC	15	0.7	0	— —	— —
BC	15	0.8	0	— —	0.86
BC	15	0.7	4	— —	— —
BC	15	0.8	4	— —	0.78

Fig. 7   PIV average velocity field for $Ma = 0.8, \alpha = 4°$ on Coe and Nute configuration. On the left streamwise velocity component, on the right vertical velocity component.

Fig. 9 Standard deviation of schlieren pixel intensity (left) and streamwise PIV velocity component (right) for $Ma = 0.8$, $\alpha = 4°$ on Coe and Nute configuration.

the shear layer region for $200\% < x/D < 270\%$. The large fluctuations of velocity in this region suggest that the reattachment location is actually not steady but is supposed to move according to the specific flow phase.

Comparing these results (obtained for $Ma = 0.8$ and $\alpha = 4°$) with other studies on the same model and under similar conditions, particularly Panda et al. [23], shows better qualitative agreement with their results at $Ma = 0.85$, rather than $Ma = 0.80$, emphasizing that in the current investigation, the model's blockage is not negligible and the effect can be roughly associated with an increase in the effective Mach number of $\Delta Ma = 0.05$.

However, the flow field shown in Fig. 7 aligns well with the wall-modelled LES results from Kenway et al. [17], where the Coe and Nute model was investigated for $Ma = 0.8$ and $\alpha = 4°$. This numerical study highlights a variation in the SW position between the leeward and windward sides of the launcher, with the SW located further upstream on the windward side (particularly evident for the 1st SW). A similar qualitative observation can be made from the results of this study, as shown in the schlieren visualization in Fig. 6, although no PIV images of the windward side are available in the present investigation. Additionally, the numerical study of Kenway et al. [17] predicts a more downstream reattachment location on the windward side compared to the leeward side of the launcher.

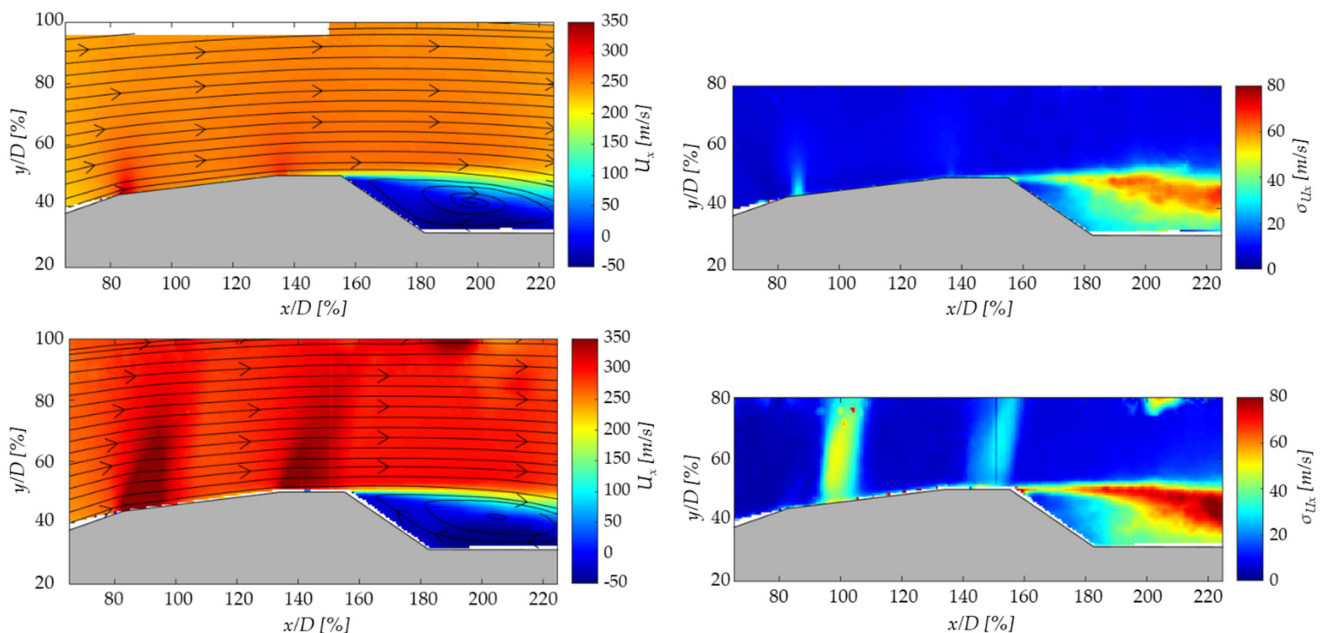### B. Effect of Flow Conditions: Angle of Attack and Mach Number

Tests at $\alpha = 0°$ (and $Ma = 0.8$) provide insights into the flow behavior in the absence of angle of attack. Comparing Figs 7, 9 and 10 (bottom), it is evident that without angle of attack, there is an increase in the range of oscillation for the 2nd shockwave and slightly more upstream shockwave locations. However, a comparable range of oscillation for the 1st shockwave structures (slightly stronger and located more upstream for $\alpha = 4°$) and for the separated area is observed. These observations are further supported by the values of average shockwave positions and their respective ranges of oscillation obtained from the schlieren images, as shown in Table 4. Similar results were obtained by Camussi et al. [9], who observed only minor variations in both shock strength and pressure fluctuations in the presence of an angle of attack.

The presence of angle of attack becomes more evident in the reattachment area, as confirmed by oil flow visualization, introducing asymmetries in the oil pattern compared to the straight orientation of streamlines for $\alpha = 0°$ (Fig. 11). Furthermore, flow reattachment is taking place slightly more downstream (about $10\%D$) in the presence of angle of attack (see Table 5) and in agreement with Coe and Nute [3].These values of the reattachment locations are also very similar to the numerical values reported by Lecler et al. [16] and Liu [14] (for $\alpha = 0°$ and $Ma = 0.81$) and the experimental data of Schuster et al. [18].

These results demonstrate that while the presence of angle of attack does not fundamentally alter the general flow behavior, it does have an impact on the characteristics of shockwaves and reattachment locations.

Tests at the lower Mach number, $Ma = 0.7$ (for $\alpha = 0°$), exhibit a reduced strength and range of oscillation for the first shockwave compared to the higher Mach number case. As expected, for this lower Mach number the 1st shockwave is located more upstream (of about $10\%D$). Interestingly, no shockwave is observable just upstream of the boat tail's top corner in the average velocity field.

Fig. 10 Average (left) and standard deviation (right) of PIV velocity field for $Ma = 0.7$, $\alpha = 0°$ (top) and $Ma = 0.8$, $\alpha = 0°$ (bottom) on Coe and Nute configuration.

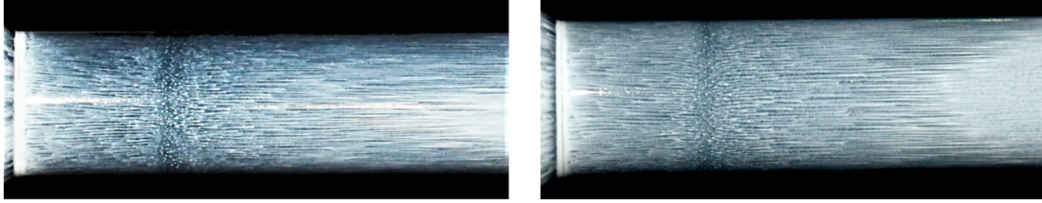**Fig. 11   Oil flow visualization for $Ma = 0.7$, $\alpha = 0°$ (left) and $Ma = 0.8$, $\alpha = 0°$ (right) on Coe and Nute configuration.**

However, in the instantaneous PIV and schlieren images (not shown here) a weak shockwave is intermittently present in that region.

Despite some fluctuations being more energetic for the higher Mach number case, the average extent of the separated area does not vary significantly between the two cases. This consistency in the extent of the recirculation region is further supported by similar reattachment locations observed through oil flow visualizations and PIV results (see Table 5 and Fig. 11).

Therefore, the effect of compressibility (increased Ma), mainly influences the formation of shockwave structures and the extent of local supersonic areas, which are only evident at the higher Mach number. For these configurations, the occurrence of stronger quasi-normal shockwave structures does not directly cause the presence of a shock foot separated area but is expected to cause an increase in the local thickness of the boundary layer. As anticipated, since the separated boat tail area is triggered by the sharp boat tail corner, no significant variation in the separated region is qualitatively observed.

Although it is not possible to directly compare these velocity field data with other experimental studies due to the lack of full-field quantitative experimental data (as experimental studies typically rely on unsteady or steady surface pressure measurements or schlieren visualizations), they can be compared with the numerical study by Liu et al. [14]. This study examines the Coe and Nute configuration at $\alpha = 0°$ for $Ma = 0.6$; 0.7; 0.81; 0.88; 1.0; 1.08. The main flow field at $Ma = 0.7$ and $Ma = 0.81$ is in good agreement with the results presented in this study for $Ma = 0.7$ and $Ma = 0.8$ respectively, however, some discrepancies are noted in the reattachment location. In Liu et al. [14], the reattachment location shifts further upstream with increasing Mach number, which is contrary to the trend observed in this manuscript. Good agreement is instead observed in terms of shockwave position, when compared to both the numerical study of Liu et al. [14] and the experimental findings of Schuster et al. [18].

To provide a more in-depth analysis, Figs. 12 and 13 depict profiles of mean and relative standard deviation of the streamwise
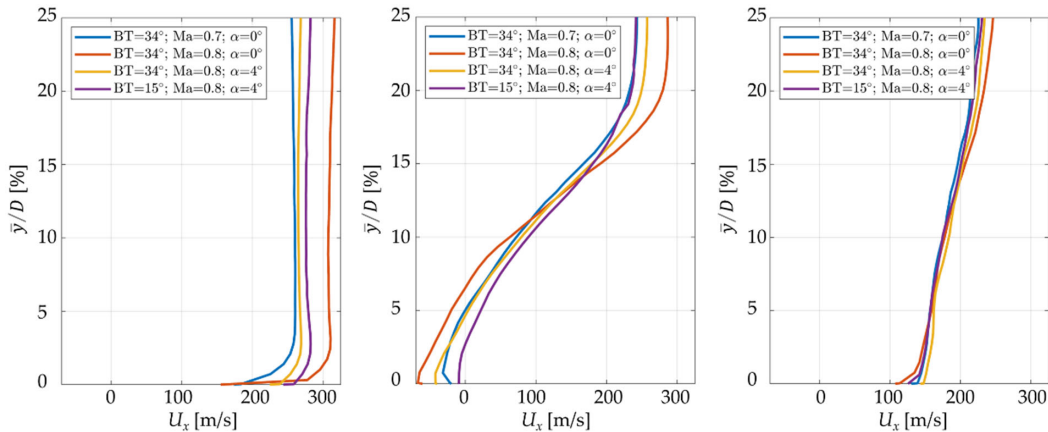

Fig. 12   Streamwise velocity profiles for four configurations and for three streamwise locations: $x/D = 154\%$ (left), $x/D = 225\%$ (center), and $x/D = 300\%$ (right). All the profiles are plotted against local nondimensional distance from the launcher surface, $\bar{y}/D$.
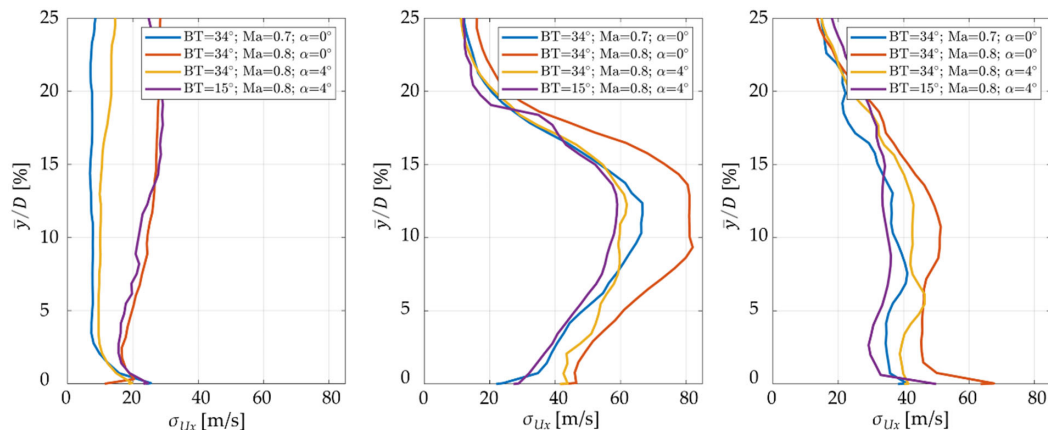

Fig. 13   Standard deviation profiles of streamwise velocity component for four configurations and for three streamwise locations: $x/D = 154\%$ (left), $x/D = 225\%$ (center), and $x/D = 300\%$ (right). All the profiles are plotted against local nondimensional distance from the launcher surface, $\bar{y}/D$.

velocity component, at three key streamwise locations: the boat tail corner ($x/D = 154\%$), the end of the 15° boat tail ($x/D = 225\%$), and downstream of the reattachment location ($x/D = 300\%$). These profiles are plotted against the local vertical distance from the launcher model, denoted as $\bar{y}$.

All the velocity profiles reveal an overall increase in velocity for the flow configuration with $Ma = 0.8$ and $\alpha = 0°$ for $\bar{y} > 15\%D$. The lower velocities observed for $\alpha = 4°$ are justified by the divergent region created between the wind tunnel top wall and the model surface in the presence of an angle of attack. This divergent region results in a deceleration of the flow field in the subsonic region of the field of view, while it leads to a faster expansion in the supersonic flow areas (resulting in a more upstream shockwave location in agreement with Table 4). Due to the closer proximity of the model to the top wall, this effect is more evident for $x/D = 154\%$. The higher velocity fluctuations at $x/D = 154\%$ (see Fig. 13, left) for $\alpha = 0°$ and $Ma = 0.8$ can be attributed to the larger range of oscillation for the 2nd SW in this configuration.

Moving to $x/D = 225\%$, a larger reverse flow area characterizes the zero angle of attack case, accompanied by increased standard deviation values. Downstream of the reattachment location ($x/D = 300\%$), similar velocity values are observed, although slightly larger for the $\alpha = 0°$ case. However, once again, higher fluctuations are still associated with the zero angle of attack case.

The velocity profiles for the $Ma = 0.7$ case confirm, despite obviously lower average velocity values, comparable velocities in the separated area with respect to the other configuration with same boat tails, albeit with significantly reduced fluctuation values.

C. Effect of Nose Geometry

Analyzing the influence of nose geometry through schlieren instantaneous and standard deviation images provides valuable insights. Instantaneous schlieren images (refer to Fig. 14) exhibit distinct variations in shockwave structures. Specifically, the bi-conic nose leads to the formation of two shockwave structures, in contrast to the single shockwave for the conic and ogive noses. This bi-conic configuration offers advantages in reducing shockwave strength, minimizing total pressure losses, and consequently influencing the size of the separated area. This is evident in the shear layer line (quasi-horizontal line), which remains flat for the bi-conic case but bends upwards for the ogive and, particularly, the conic cases. Flow separation for the bi-conic case initiates at the boat tail corner, while for the other two cases, it occurs slightly more upstream, at the

shock foot. Additionally, the expansion fan for the bi-conic and conic cases is localized in the geometry transition locations, while for the ogive (SH) case, it is distributed over a larger area (see expansion waves in Fig. 14, right).

The standard deviation plot in Fig. 15 further supports these observations, indicating a larger range of shockwave oscillation for the conic and ogive cases compared to the bi-conic case. Consequently, higher energy appears associated with the fluctuation of the shear layer for the two single-shockwave cases. These findings align with Ericsson's work [7], which demonstrated a mitigation of flow unsteadiness and aeroelastic instabilities when using a bi-conic nose compared to a conic case.

For an assessment of the dynamic behavior of shockwave structures, the time evolution of a single horizontal pixel line (at a distance of 0.5 cm from the surface of the model) in the schlieren images is presented in Fig. 16. The analysis focuses on a specific region ($50 < x/D < 200\%$) and spans approximately $\Delta t = 0.02$ s. A comparison between the bi-conic (left), conic (center), and SH (right) nose configurations (all with a boat tail angle of 34°) reveals several noteworthy observations. In the case of the conic nose, there is a larger range of oscillation for the shockwave structure, a trend consistent with the quantitative data outlined in Table 4. Between the conic and SH nose configurations, a more periodic behavior is observed for the latter, characterized by cycles of oscillation with similar amplitude, while larger variations between cycles are evident for the conic case. Additionally, the shockwave line appears thicker in the conic configuration compared to the other two fairing configurations, suggesting the presence of substantial density variations integrated along the line of sight. This phenomenon is likely associated with the initiation of the separated area at the shock foot for the conic case. Consequently, the intrinsic three-dimensionality of the separated area contributes to variations in the shockwave position along the circumferential direction of the model. The thicker shockwave line can also be linked to a larger λ-structure for the conic configuration. Differently, the SH and the bi-conic configurations show similarities in the dynamics of the shockwave upstream of the boat tail region, both in terms of streamwise amplitude and oscillation period.

To provide a visual representation of the impact of different nose geometries on the separated area and reattachment location, oil flow images are depicted in Fig. 17. The illustrations showcase a consistent reattachment location for the bi-conic and ogive cases, contrasted by a notably more downstream reattachment location in the
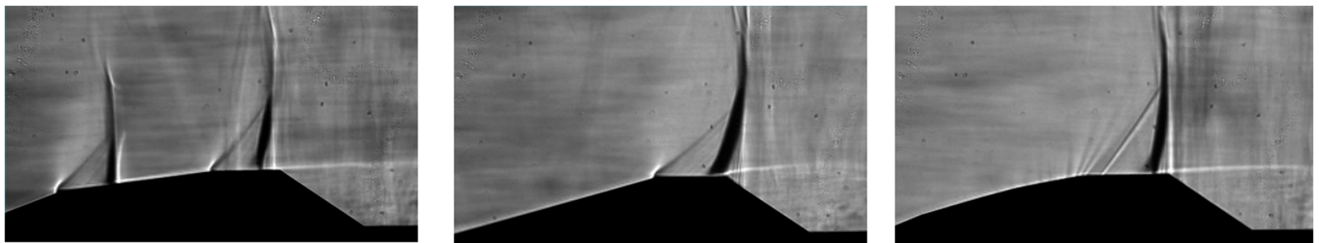

Fig. 14 Instantaneous schlieren snapshot for $Ma = 0.8$, $\alpha = 0°$ for bi-conic (left), conic (center) and Sears-Haack (right) noses in presence of a boat tail of 34°.
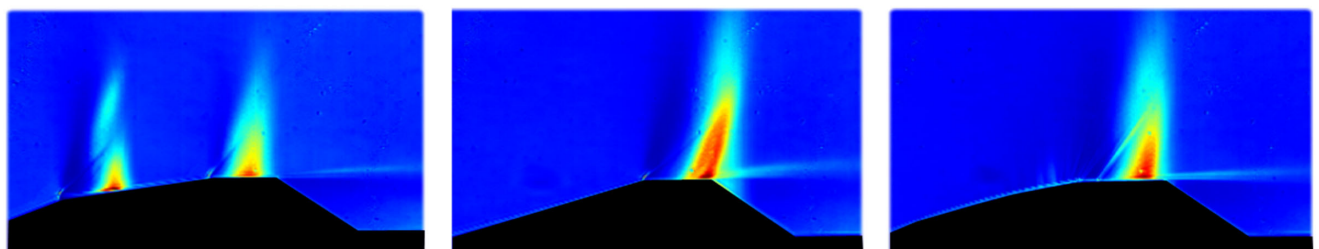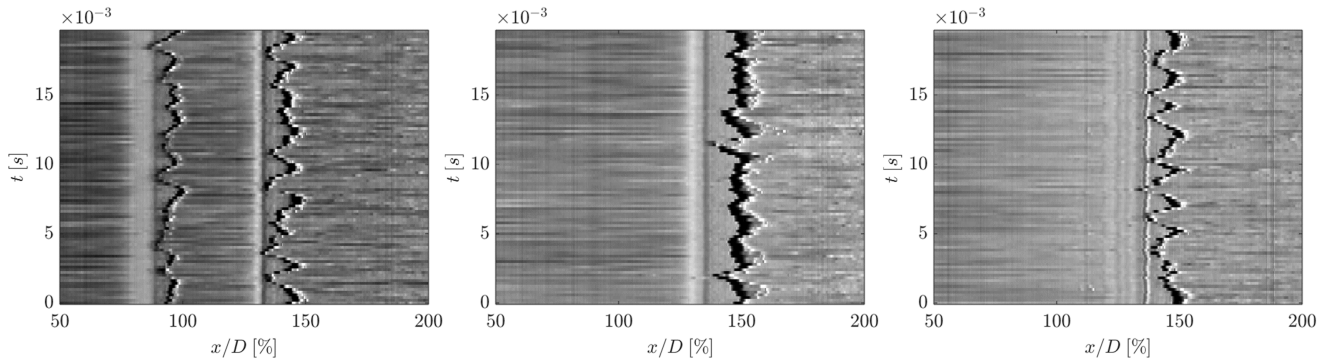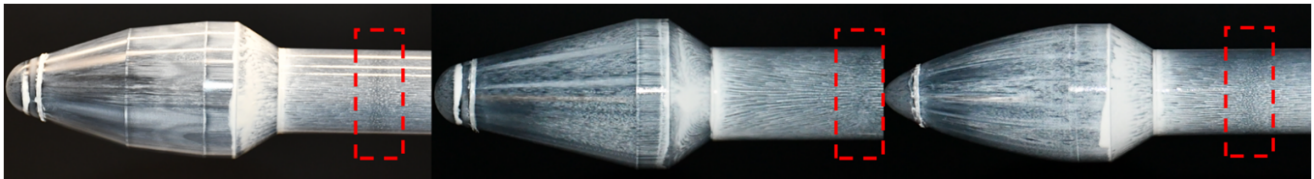

Fig. 15 Standard deviation of schlieren images for $Ma = 0.8$, $\alpha = 0°$ for bi-conic (left), conic (center) and Sears-Haack (right) noses in presence of a boat tail of 34°.

Fig. 16 Time behavior of schlieren pixel line intensity in the SW oscillation ranges for $Ma = 0.8$, $\alpha = 0°$ for bi-conic (left), conic (center) and Sears-Haack (right) noses in presence of a boat tail of 34°.

Fig. 17 Oil flow visualization for $Ma = 0.8$, $\alpha = 0°$ for bi-conic (left), conic (center) and Sears-Haack (right) noses in presence of a boat tail of 34°.

case of the conic nose, as confirmed by the data reported in Table 5. This evidence reaffirms that the conic configuration leads to a more extensive separated area and, consequently, greater pressure losses.

The reattachment location manifests as a distinct darker area, exhibiting a coherent pattern along the circumferential direction for the bi-conic and ogive configurations. However, the reattachment location is less discernible for the conic case, likely attributed to higher fluctuations in this configuration, resulting in a broader range of reattachment locations (considering consistent oil application across configurations).

For the different configurations, reattachment takes place between 0.8 and 1.3D downstream of the boat tail corner ($x/D = 154\%$) (4–7 step height). These results closely align with Schrijer et al. [6], who observed a reattachment location at 1.0D for a backward facing step case. Slightly more downstream reattachment locations are found in Hudy et al. [35], while Gentile et al. [36] analyzed different afterbody diameters and reported reattachment locations between 0.8D and 1D for the different configurations investigated.

D. Boat Tail Effect

To explore the boat tail effect, the bi-conic nose case is kept constant, while three different boat tails with angles of 5°, 15°, and 34° are analyzed using schlieren and PIV results.
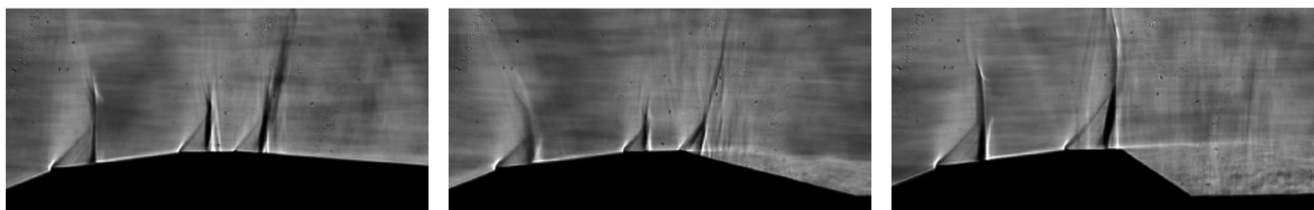
The images in Fig. 18 (for $Ma = 0.8$ and $\alpha = 0°$) illustrate that only in the case of the 34° boat tail is a separated area triggered at the boat tail corner. For the other cases, the change in flow direction does not abruptly cause flow separation. The gentler variation in the orientation of the flow streamlines results in a third localized expansion region at the boat tail top corner, leading to the occurrence of a further (third) supersonic area and an additional shockwave structure. The absence of a separated area at the boat tail corner leads also to a less-dissipative shockwave structure upstream of the boat tail

upper corner (2nd SW). It is noteworthy that the presence of the third shockwave structure is intermittent and depends on the position of the secondary shockwave structure. This variability is well illustrated by the time history of pixel intensity in the schlieren images shown in Fig. 19. Specifically, for a boat tail angle of 5°, the occurrence of a third shockwave structure downstream of the boat tail corner ($x/D > 154\%$) is observed during specific flow phases only.
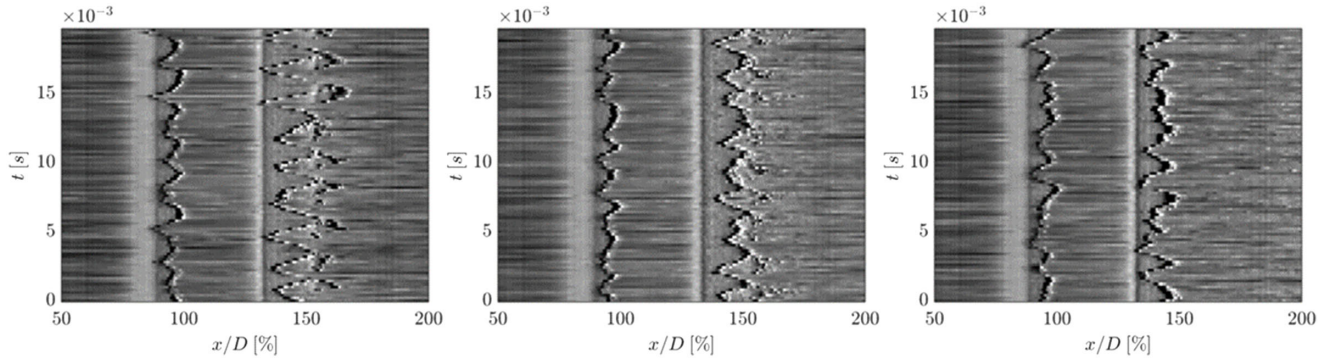
In detail, as the second shockwave starts moving downstream from the most upstream position, its strength reduces as the shockwave proceeds in the same direction as the flow. Under these conditions, the flow has the opportunity to re-accelerate across the boat tail corner, leading to the formation of a third shockwave structure. As the second shockwave approaches the most downstream location, a more dissipative SW structure is present, causing the third shockwave to progressively move upstream. Eventually, the two shockwaves merge at the most downstream location of the second shockwave. Due to the increased strength of the second shockwave, no additional shockwave appears during its entire upstream travel. A similar behavior is also present for the intermediate boat tail case (15°), although in this scenario, the occurrence of the third shockwave is less prominent due to the larger angle variation encountered by the flow (with respect to the 5° boat tail). However, even in this case, the third shockwave structure is observed only during the downstream travel of the second shockwave.

Downstream of the shockwaves (see Fig. 18), a smaller separated area is triggered for the 15° case compared to the Coe and Nute 34° boat tail, while no separation is observed in the schlieren images for the 5° case.

To provide a detailed analysis of the separated area, average PIV images for the streamwise velocity component are shown in Fig. 20 for an angle of attack of 4° and $Ma = 0.8$ for the 34° and 15° boat tails only (no PIV investigation was carried out for the 5° boat tail).

Fig. 18 Instantaneous schlieren snapshot for $Ma = 0.8$, $\alpha = 0°$ for boat tails of 5° (left), 15° (center) and 34° (right) in presence of a bi-conic nose.

Fig. 19 Time behavior of schlieren pixel line intensity in the SW oscillation ranges for $Ma = 0.8$, $\alpha = 0°$ for boat tails of 5° (left), 15° (center) and 34° (right) in presence of a bi-conic nose.

Figure 20 also highlights the region of the average reverse flow area (depicted in purple) for both boat tails investigated with PIV. The plot illustrates that for the 15° boat tail, the region of the average reverse flow is much smaller.

However, since the separated flow is highly unsteady, it is more appropriate to discuss the probability of reverse flow, P_{rev}, defined for each spatial vector as the percentage of snapshots in which a negative velocity was experienced. This approach aligns with the methodology of Giepman et al. [37]. The results (Fig. 21) show a higher probability of separation for the larger boat tail angle case, with a significant area having a separation probability higher than 90%. In contrast, for the 15° boat tail case, the probability of separation is higher than 50% only in a small area. The plot of P_{rev} for the 34° BT case includes an oblique black dashed line corresponding to the location of the boat tail for the 15° case for reference. Even when considering only the area common to the two boat tail cases (region above the dashed oblique line), a higher probability of separation is still evident for the larger boat tail case.

From the probability of separation, the extent of the separated area (A_{Sep}) is computed through spatial integration of P_{rev} in the region between $160\% < x/D < 270\%$ and $13\% < y/D < 40\%$. The extent of A_{Sep}, with respect to the entire integration area, is 24% for the boat tail of 34°, while it is less than half (10%) for the lower angle boat tail. When restricting the spatial integration to only the region in common between the two cases (area above the dashed black line in Fig. 20), $A_{Sep} = 13\%$ for the 34° boat tail case. This confirms the previous qualitative observation of an increase in separated area compared to the 15° case in this subregion as well.
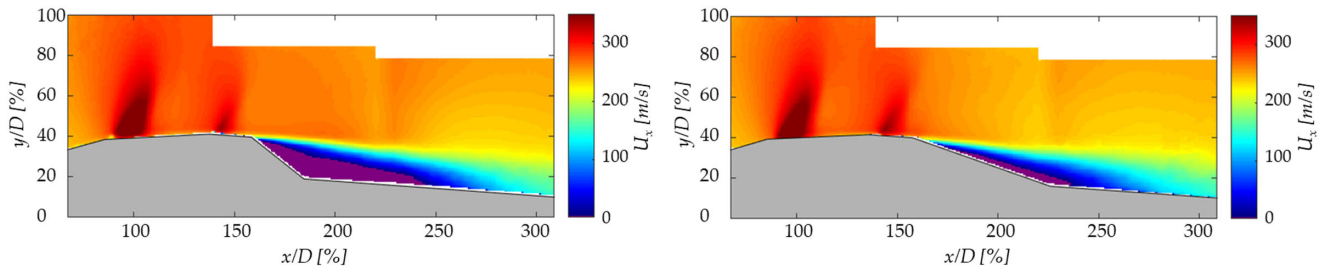
These differences are also confirmed by the velocity profiles in Figs. 12 and 13, which show reduced reverse flow velocity and fluctuations for the 15° BT compared to the Coe and Nute case, except higher fluctuations at the boat tail corner (Fig. 13, left, purple vs yellow line). The higher fluctuations in this region are associated with a larger range of shockwave oscillation, which, in some cases, extends downstream of the boat tail corner (see Fig. 18). Very similar velocity profiles between the 34° and the 15° boat tail cases (both for $Ma = 0.8$ and $\alpha = 4°$) are instead retrieved downstream of the reattachment location ($x/D = 300\%$).

Therefore, it is confirmed that a more gradual geometry variation at the boat tail (present for the 5° and the 15° boat tail cases) helps to reduce the velocity fluctuations and, consequently, the unsteady pressure loads.
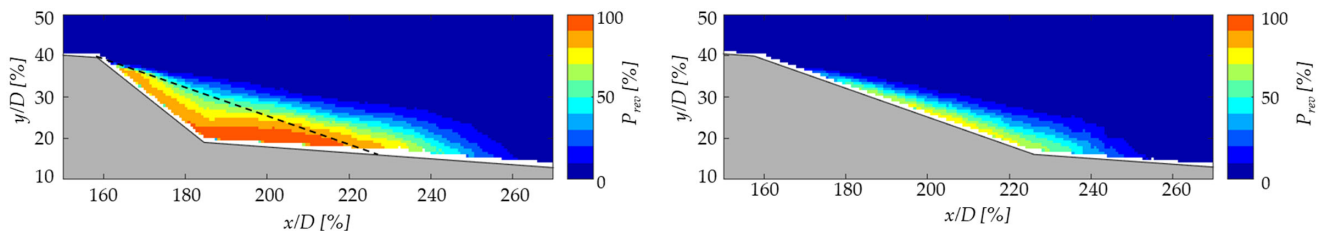
Despite the reduced probability of separation, the results in Table 5 confirm that the streamwise location of the reattachment location does not vary significantly between the two configurations. In both cases, L is approximately in the range of [0.78-0.86] for $Ma = 0.8$ and for both angles of attack.

IV. Conclusions

This study has revealed the impact of the nose and boat tail on a hammerhead launcher configuration concerning the main flow features and unsteadiness under various transonic flow conditions ($Ma = 0.7 - 0.8$ and $\alpha = 0 - 4°$). The most significant flow unsteadiness is observed in the shockwave oscillation region(s) and in the boat tail area.

Fig. 20 Streamwise average velocity field for $Ma = 0.8$, $\alpha = 4°$ for boat tails of 34° (left) and 15° (right) in presence of a bi-conic nose. The purple region indicates $U_x < 0$.

Fig. 21 Probability of reverse flow for $Ma = 0.8$, $\alpha = 4°$ for boat tails of 34° (left) and 15° (right) in presence of a bi-conic nose.

Tests at different Mach numbers showed that for the analyzed model geometries, shockwave formation already takes place at $Ma = 0.7$ and $\alpha = 0°$, intensifying at $Ma = 0.8$. For the Coe and Nute reference configuration (bi-conic nose and 34° boat tail), the Mach number does not significantly affect the average extent of the separated area but does influence the relevance of flow unsteadiness. This behavior is expected, as the separated area in this configuration is mainly induced by the boat tail geometry rather than from the occurrence of a shockwave boundary layer interaction. However, the higher Mach number case triggers large amplitude oscillations in shockwaves, exciting the pulsation of the separated area.

Comparing various nose geometries confirms Ericsson's conclusion [7] that the conic nose leads to higher flow unsteadiness and more pressure losses, while similar results are obtained for the bi-conic and Sears-Haack configurations. However, the Sears-Haack case is associated with a slightly larger shockwave oscillation range (than the bi-conic case), located just upstream of the boat tail area, potentially negatively affecting fluctuations in the separated area region.

The investigation into the boat-tail geometry highlights that a 5° or 15° boat tail suppresses or significantly reduces the separated area compared to the 34° boat tail case (reduced by 58% for the 15° case). However, the lower angle boat tail also introduces a third shockwave structure, whose oscillations pose additional challenges to the launcher's structural integrity.

It is worth noting that, for the various configurations, the nature of the boat tail separated area differs. For the Coe and Nute configurations, the separation is triggered at the boat tail corner, whereas for the cone and ogive noses, or the bi-conic nose paired with a 15° boat tail (albeit in an intermittent manner), it is caused by a shockwave-boundary layer interaction. While this study highlights how these geometric variations impact the primary flow statistics (mean and standard deviation), future investigations could explore the spectral variations associated with the dynamics of the different flow fields.

In addition to reducing the separated area and unsteady loads, the choice of an optimized launcher geometry should also consider the ratio between payload storage capacity and structure weight. Among the tested configurations, this ratio is certainly increased for the larger boat tail case. While a final decision on a specific launcher geometry would necessitate a more detailed parametric study, also including the mechanical aspects of the construction, the results presented offer valuable insights into the impact of these geometric parameters on the aerodynamic performance. PIV has enabled the quantification of the effects of these geometry variations on the entire launcher velocity field, complementing the qualitative conclusions derived from oil flow and schlieren visualizations.

Acknowledgment

References

[1] de Medeiros, J. G., Avelar, A. C., and Falcão Filho, J. B. P., "Experimental Study of Geometric Variations Effect on the Flow Patterns on a Hammerhead Satellite Launch Vehicle," *30th Congress of the International Council of the Aeronautical Sciences, International Council of the Aeronautical Sciences*, ICAS Paper 2016-0683, 2016.

[2] Suresh, B. N., and Sivan, K., *Integrated Design for Space Transportation System*, Springer, Berlin, 2015, pp. 391–454.
https://doi.org/10.1007/978-81-322-2532-4

[3] Coe, C. F., and Nute, J. B., "Steady and Fluctuating Pressures at Transonic Speeds on Hammerhead Launch Vehicles," NASA TM X-778, Dec. 1962.

[4] Dods, J. B., Jr., and Coe, C. F., "Crossflow Effects on Steady and Fluctuating Pressures on an Ogive-Cylinder Cone-Frustum Model in Supersonic Separated Flow," NASA TP-1951-A-8563, 1981.

[5] Rainey, A. G., "Progress on the Launch-Vehicle Buffeting Problem," *Journal of Spacecraft and Rockets*, Vol. 2, No. 3, 1965, pp. 289–299.
https://doi.org/10.2514/3.28174

[6] Schrijer, F. F. J., Sciacchitano, A., and Scarano, F., "Spatio-Temporal and Modal Analysis of Unsteady Fluctuations in a High-Subsonic Base Flow," *Physics of Fluids*, Vol. 26, No. 8, 2014.
https://doi.org/10.1063/1.4891257

[7] Ericsson, L. E., "Hammerhead Wake Effects on Elastic Vehicle Dynamics," *Journal of Spacecraft and Rockets*, Vol. 34, No. 2, 1997, pp. 145–151.
https://doi.org/10.2514/2.3193

[8] Cole, H. A., Erickson, A. L., and Rainey, A. G., "Buffeting During Atmospheric Ascent – Space Vehicle Design Criteria/Structures," NASA SP-8001, Nov. 1970.

[9] Camussi, R., Guj, G., Imperatore, B., Pizzicaroli, A., and Perigo, D., "Wall Pressure Fluctuations Induced by Transonic Boundary Layers on a Launcher Model," *Aerospace Science and Technology*, Vol. 11, No. 5, 2007, pp. 349–359.
https://doi.org/10.1016/j.ast.2007.01.004

[10] Imperatore, B., Guj, G., Ragni, A., Pizzicaroli, A., and Giulietti, E., "Aeroacoustic of the VEGA Launcher: Wind Tunnel Tests and Full Scale Extrapolations," *11th AIAA/CEAS Aeroacoustics Conference*, AIAA Paper 2005-2913, 2005.
https://doi.org/10.2514/6.2005-2913

[11] Kim, Y., Nam, H., Kim, J., and Sun, C., "Pressure Fluctuations on Hammerhead Vehicle at Transonic Speeds Using CFD and Semi-Empirical Formula Considering Spatial Distribution," *Journal of the Korean Society for Aeronautical & Space Sciences*, Vol. 49, No. 6, 2021, pp. 457–464.
https://doi.org/10.5139/JKSAS.2021.49.6.457

[12] Panda, J., "Aeroacoustics of Space Vehicles," *Stanford Fluid Mechanics Seminar*, ARC-E-DAA-TN12911, 2014.

[13] Troclet, B., and Depuydt, M., "Experience Learned from ARIANE 5 Wind Tunnel Tests Regarding Aerodynamic Noise on Upper Part and Buffeting Loads on Rear Part," *29th Internal Conference and Exhibition on Noise Control Engineering*, Inst. of Noise Control Engineering, Nice, France, Paper IN2000/794, 2000, pp. 27–20.

[14] Liu, Y., Wang, G., Zhu, H., and Ye, Z., "Numerical Analysis of Transonic Buffet Flow Around a Hammerhead Payload Fairing," *Aerospace Science and Technology*, Vol. 84, Jan. 2019, pp. 604–619.
https://doi.org/10.1016/j.ast.2018.11.002

[15] Murman, S. M., and Diosady, L., "Simulation of a Hammerhead Payload Fairing in the Transonic Regime," *54th AIAA Aerospace Sciences Meeting*, AIAA Paper 2016-1548, 2016.
https://doi.org/10.2514/6.2016-1548

[16] Lecler, S., Weiss, P. E., and Deck, S., "Prediction of Wall-Pressure Fluctuations for Separating/Reattaching Flows Applied to Space Launchers Using Zonal Detached Eddy Simulation-Based Convolutional Neural Networks," *Physics of Fluids*, Vol. 35, No. 6, 2023, Paper 065107.
https://doi.org/10.1063/5.0146358

[17] Kenway, G. K., Ghate, A., Browne, O. M. F., Wong, M. L., Angel, J. B., and Kiris, C. C., "Immersed Boundary Wall-Modelled Large Eddy Simulations of a Generic Hammerhead Payload Fairing," *AIAA Aviation Forum and ASCEND 2024*, AIAA Paper 2024-3693, 2024.
https://doi.org/10.2514/6.2024-3693

[18] Schuster, D. M., Panda, J., Ross, J. C., Roozeboom, N. H., Burnside, N. J., Ngo, C. L., Sellers, M., and Powell, J. M., "Investigation of Unsteady Pressure-Sensitive Paint (uPSP) and a Dynamic Loads Balance to Predict Launch Vehicle Buffet Environments," NASA TM-2016-219352, 2016.

[19] Coe, C. F., "The Effects of Some Variations in Launch-Vehicle Nose Shape on Steady and Fluctuating Pressures at Transonic Speeds," NASA TM-X-646, 1962.

[20] Kumar, R., Viswanath, P. R., and Prabhu, A., "Mean and Fluctuating Pressure Field in Boat Tail Separated Flows at Transonic Speeds," *39th Aerospace Sciences Meeting and Exhibit*, AIAA Paper 2001-0582, 2001.
https://doi.org/10.2514/6.2001-582

[21] Sachdeva, A., Malik, M. S., and Priyadarshi, P., "Boat-Tail Shape Optimization Studies for a Payload Fairing," *Symposium on Applied Aerodynamics and Design of Aerospace Vehicle*, SAROD CP-019, Dec. 2015.

[22] Sunil, K., Johri, I., and Priyadarshi, P., "Aerodynamic Shape Optimization of Payload Fairing Boat Tail for Various Diameter Ratios," *Journal of Spacecraft and Rockets*, Vol. 59, No. 4, 2022, pp. 1–14.
https://doi.org/10.2514/1.A35215

[23] Panda, J., Garbeff, T., Burnside, N., and Ross, J., "Unsteady Pressure Fluctuations Measured on a Hammerhead Space Vehicle and Comparison with Coe and Nute's 1962 Data," *International Journal of Aeroacoustics*, Vol. 17, Nos. 1–2, 2018, pp. 70–87.
https://doi.org/10.1177/1475472X17743626

[24] Ericsson, L. E., and French, N. J., "The Aeroelastic Characteristics of the Saturn IB SA-203 Launch Vehicle," NASA CR-76563, April 1966.

[25] Garbeff, T. J., Panda, J., Ross, J. C., and Smith, N. T., "Experimental Visualizations of a Generic Launch Vehicle Flow Field: Time-Resolved Shadowgraph and Infrared Imaging," *55th AIAA Aerospace Sciences Meeting*, AIAA Paper 2017-1403, 2017.
https://doi.org/10.2514/6.2017-1403

[26] Nicolì, A., Imperatore, B., Fauci, R., and Pizzicaroli, A., "Wind Tunnel Test Campaigns of the VEGA Launcher," *44th AIAA Aerospace Sciences Meeting and Exhibit*, AIAA Paper 2006-0257, 2006.
https://doi.org/10.2514/6.2006-257

[27] Pope, A., and Goin, K. L., *High-Speed Wind Tunnel Testing*, Wiley, New York, 1965, p. 320.
https://doi.org/10.1017/S0001924000057213

[28] D'Aguanno, A., "Physics and Control of Transonic Buffet," Ph.D. Thesis, Delft Univ. of Technology, Delft, The Netherlands, Jan. 2023.
https://doi.org/10.4233/uuid:7e4f868b-7716-4c36-8fa0-b55572d1572b

[29] Settles, G. S., "Toepler's Schlieren Technique, Schlieren and Shadowgraph Techniques," *Experimental Fluid Mechanics*, Springer, Berlin, 2001.
https://doi.org/10.1007/978-3-642-56640-0_3

[30] Westerweel, J., and Scarano, F., "Universal Outlier Detection for PIV Data," *Experiments in Fluids*, Vol. 39, No. 6, 2005, pp. 1096–1100.
https://doi.org/10.1007/s00348-005-0016-6

[31] Humble, R. A., "Unsteady Flow Organization of a Shock Wave/Boundary Layer Interaction," Ph.D. Thesis, Delft Univ. of Technology, Delft, The Netherlands, 2009.

[32] Ragni, D., Schrijer, F. F. J., van Oudheusden, B. W., and Scarano, F., "Particle Tracer Response Across Shocks Measured by PIV," *Experiments in Fluids*, Vol. 50, No. 1, 2011, pp. 53–64.
https://doi.org/10.1007/s00348-010-0892-2

[33] D'Aguanno, A., Schrijer, F. F. J., and van Oudheusden, B. W., "Experimental Investigation of the Transonic Buffet Cycle on a Supercritical Airfoil," *Experiments in Fluids*, Vol. 62, No. 214, 2021.
https://doi.org/10.1007/s00348-021-03319-z

[34] Camussi, R., Di Marco, A., Stoica, C., Bernardini, M., Stella, F., De Gregorio, F., Paglia, F., Romano, L., and Barbagallo, D., "Wind Tunnel Measurements of the Surface Pressure Fluctuations On the New VEGA-C Space Launcher," *Aerospace Science and Technology*, Vol. 99, April 2020, Paper 105772.
https://doi.org/10.1016/j.ast.2020.105772

[35] Hudy, L. M., Naguib, A., Humphreys, W., and Bartram, S., "Particle Image Velocimetry Measurements of a Two/Three-Dimensional Separating/Reattaching Boundary Layer Downstream of an Axisymmetric Backward-Facing Step," *43rd AIAA Aerospace Sciences Meeting and Exhibit*, AIAA Paper 2005-0114, 2005.
https://doi.org/10.2514/6.2005-114

[36] Gentile, V., Schrijer, F. F. J., van Oudheusden, B. W., and Scarano, F., "Afterbody Effects on Axisymmetric Base Flows," *AIAA Journal*, Vol. 54, No. 8, 2016, pp. 2285–2294.
https://doi.org/10.2514/1.J054733

[37] Giepman, R. H. M., Schrijer, F. F. J., and van Oudheusden, B. W., "A Parametric Study of Laminar and Transitional Oblique Shock Wave Reflections," *Journal of Fluid Mechanics*, Vol. 844, April 2018, pp. 187–215.
https://doi.org/10.1017/jfm.2018.165